

Universality class of the motility-induced critical point in large scale off-lattice simulations of active particles

Claudio Maggi^{1,2,*}, Matteo Paoluzzi³, Andrea Crisanti^{2,4}, Emanuela Zaccarelli^{4,2}, and Nicoletta Gnan^{4,2†}

¹*NANOTEC-CNR, Institute of Nanotechnology,
Soft and Living Matter Laboratory, Roma, Italy*

²*Dipartimento di Fisica, Sapienza Università di Roma,
Piazzale A. Moro 2, I-00185, Rome, Italy*

³*Departament de Física de la Matèria Condensada,
Universitat de Barcelona,*

C. Mart Franquès 1, 08028 Barcelona, Spain

⁴*CNR-ISC, Institute of Complex Systems, Roma, Italy*

We perform large-scale computer simulations of an off-lattice two-dimensional model of active particles undergoing a motility-induced phase separation (MIPS) to investigate the systems critical behaviour close to the critical point of the MIPS curve. By sampling steady-state configurations for large system sizes and performing finite size scaling analysis we provide exhaustive evidence that the critical behaviour of this active system belongs to the Ising universality class.

Introduction. One of the pillars of statistical physics is the concept of universality in critical phenomena. In equilibrium systems, close to a second-order phase transition, universality can be ultimately attributed to the divergence of the correlation length of the order parameter. The behavior of this growing length-scale is found to be independent on the microscopic details of the systems but is determined only by few specific features, i.e. the spatial dimensionality and the symmetries of the order parameter as firstly hypothesized by Kadanoff [1]. Depending on such parameters it is possible to trace back the critical behaviour of disparate systems within few groups, called universality classes.

One of the biggest challenge of recent years is to transfer the vast knowledge acquired on universal behaviour of equilibrium systems into active matter physics. Active matter represents a peculiar class of non-equilibrium systems where the elementary units or agents are self-propelled objects capable to convert energy in systematic movement [2, 3]. The interacting agents are often complex biological objects that exhibit self-organized behavior at large scales giving rise to many and diverse Living Materials [4]. In particular, self-propulsion can trigger a feedback between motility and local density causing an effective attractive interaction between active particles [5]. This attractive force can bring to a phase separation in active fluids remarkably similar to the gas-liquid coexistence in equilibrium systems. Such a mechanism is usually called Motility-Induced Phase Separation (MIPS) [6]. Since MIPS is a very general feature of active dynamics, observed independently on the details of the self-propulsion, it might play a role also in biological systems. For instance, it has been recently observed that multicellular aggregates of *Myxococcus xanthus* might take advantage of density-motility feedback

for developing large scale collective behaviors that have been well described by MIPS [7].

In equilibrium physics the standard gas-liquid coexistence ends with a critical point that belongs to the Ising universality class [8, 9]. A natural question is whether or not MIPS curve ends in a critical point and if there is a region close to phase separation in which active systems display a critical behaviour that can be traced back to a specific universality class. Effective equilibrium approaches [10, 11], numerical simulations on lattice and field-theoretic computations [12] point to the Ising universality class. Despite numerous investigations have addressed the properties phase-separated MIPS states [13–20], the numerical study of the critical region and the determination of the critical properties remain still challenging and controversial. In particular it has been shown that critical active Brownian particles in two-dimensions ($2d$) display some critical exponents deviating considerably from the Ising critical exponents [21]. However recent numerical studies of an active model on a lattice have shown that critical exponents are in good agreement with the Ising universality class [12] and suggested that simulations done off-lattice have been performed far from the scaling regime due to the small size of the systems.

In this Letter, we report results from large-scale off-lattice numerical simulations of Active Ornstein-Uhlenbeck particles (AOUPs) at criticality. Combining massive simulations on GPU and Finite-Size-Scaling (FSS) analysis, we show that the system’s critical exponents agree with the Ising universality class.

Model and Methods. We consider a system composed of N self-propelled AOUP disks in $2d$ [22, 23]. This model is perhaps the simplest active particle model (due to the linearity of the process producing the “active noise”) which has lead to numerous novel theoretical developments [24–26]. It has been shown [24] that AOUPs exhibit MIPS for large values of the persistence time of the activity, as also displayed in Fig. 1(a)-(d). The equations of motion of AOUPs read

* claudio.maggi@roma1.infn.it

† nicoletta.gnan@roma1.infn.it

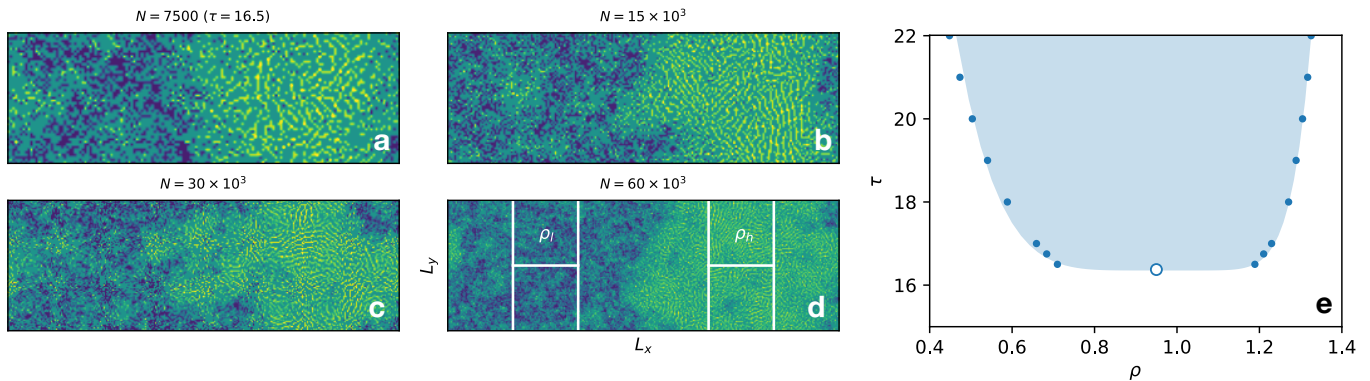


FIG. 1. (a)-(d) Density field in a slab geometry for four active systems of different sizes at $\tau = 16.5$ (where phase separation becomes appreciable). The color map encodes the local density value from yellow (high density) to blue (low density). The configurations have been shifted so that the dense and diluted phases are centered onto the four sub-boxes (panel (d)) considered in the analysis. The average density in the left sub-boxes is denoted by ρ_l (the density of the low-density phase), while the average density of the right sub-boxes by ρ_h (high-density). (e) Coexistence curve constructed with the densities of the dense and diluted phases (filled data-points), the estimated critical point is shown as an open circle.

$$\dot{\mathbf{r}}_i = \boldsymbol{\psi}_i + \mathbf{F}_i \quad (1)$$

$$\tau \dot{\boldsymbol{\psi}}_i = -\boldsymbol{\psi}_i + \boldsymbol{\eta}_i \quad (2)$$

where we indicate with \mathbf{r}_i the i -th particle's position, with $\boldsymbol{\psi}_i$ the self-propelling force, and with $\mathbf{F}_i = \sum_{j \neq i} \mathbf{f}_{ij}$ the conservative force acting on the particle. We consider two-body interactions, i.e., $\mathbf{f}_{ij} = -\nabla_{\mathbf{r}_i} \phi(r_{ij})$, with $r_{ij} = |\mathbf{r}_i - \mathbf{r}_j|$ and use a simple steep repulsive potential $\phi(r) = (r/\sigma)^{-12}/12$ (the inverse power-law potential) with a cut-off at $r = 2.5\sigma$. Here σ represents the diameter of the particle and is set to 1. In Eq. (2) $\boldsymbol{\eta}$ is a standard white noise source, i.e. $\langle \eta_i^\alpha(t) \rangle = 0$ and $\langle \eta_i^\alpha(t) \eta_j^\beta(s) \rangle = 2D \delta_{ij} \delta^{\alpha\beta} \delta(t-s)$, where the greek indices indicate Cartesian components. Here τ is the persistence time of the active force and D is the diffusivity of the non-interacting particles which is related to the mean squared velocity v by $D = v^2 \tau$. In all simulations we fix $v = 1$ and increase τ from small to large values to observe the transition as shown by the schematic phase diagram in Fig. 1(e). Eq.s (1),(2) have been integrated numerically using the Euler scheme with a time step $\Delta t = 10^{-3}$ up to $N_t = 10^9$ time steps for the largest systems: such a long time is adequate to observe full relaxation of the density auto-correlation function as shown in the Supplemental Material (SM). In addition we start each simulation from a random initial configuration and we perform up to $N_e = 10^8$ equilibration steps which guarantees that all runs reach the steady-state, even close to the critical point. We perform averages over several independent runs and errors reported represent twice the standard error of the mean (see SM for details).

The active particles move in a rectangular box of size $L_x \times L_y$ with 1:3 ratio ($L_x = 3L_y$) and periodic boundary conditions. The simulated systems size are $N = (7.5, 15, 30, 60) \times 10^3$.

To avoid spurious effects due to the presence of an interface [21, 27] we compute the quantities of interest only in four sub-boxes of size $L = L_y/2$ centered on the dense and diluted phases. These boxes are located at $x = L_x/2 \pm L_x/4$ and at $y = L_y/2 \pm L_y/4$. To ensure that these positions coincide with the locations of the dense and diluted phases, as in [21], for each configuration we first find the system center of mass along x (with periodic boundaries [28]), and we shift all particles so that the x -coordinate of the center of mass coincides with $x = L_x/2 + L_x/4$ as shown in Fig. 1(d). All simulations are performed at the fixed density $\rho = 0.95$ by varying accordingly the box size $L_x = 3L_y = (3N/\rho)^{1/2}$. $\rho = 0.95$ corresponds approximately to the critical density estimated for the smallest system size investigated (see SM for details).

Results. Although finite systems can not develop any diverging correlation length, the finite-size scaling hypothesis allows us to systematically study the critical properties away from the thermodynamic limit [29]. Using the finite-size scaling ansatz, we assume that a generic observable \mathcal{O} near the critical point behaves as

$$\mathcal{O} = L^{\frac{\zeta_{\mathcal{O}}}{\nu}} [F_{\mathcal{O}}(L\xi^{-1}) + O(L^{-\omega}, \xi^{-\omega})], \quad (3)$$

where $\zeta_{\mathcal{O}}$ is the critical exponent associated with the observable \mathcal{O} , $F_{\mathcal{O}}$ is a universal finite-size scaling function and ω is the power of the (subleading) correction-to-scaling exponent [29]. Here ν is the exponent associated with the divergence of the correlation length ξ as the control parameter is varied across the transition. In our active particle system the relaxation time of the noise τ is the control parameter, therefore we assume $\xi \sim (\tau - \tau_c)^{-\nu}$. Using this in Eq. (3) and ignoring subleading corrections we get $\mathcal{O} = L^{\zeta_{\mathcal{O}}/\nu} G_{\mathcal{O}}(L^{1/\nu}(\tau - \tau_c))$ (where $G_{\mathcal{O}}$ is a universal scaling function). This implies that, if the correct τ_c , ν and $\zeta_{\mathcal{O}}$ are known, all values

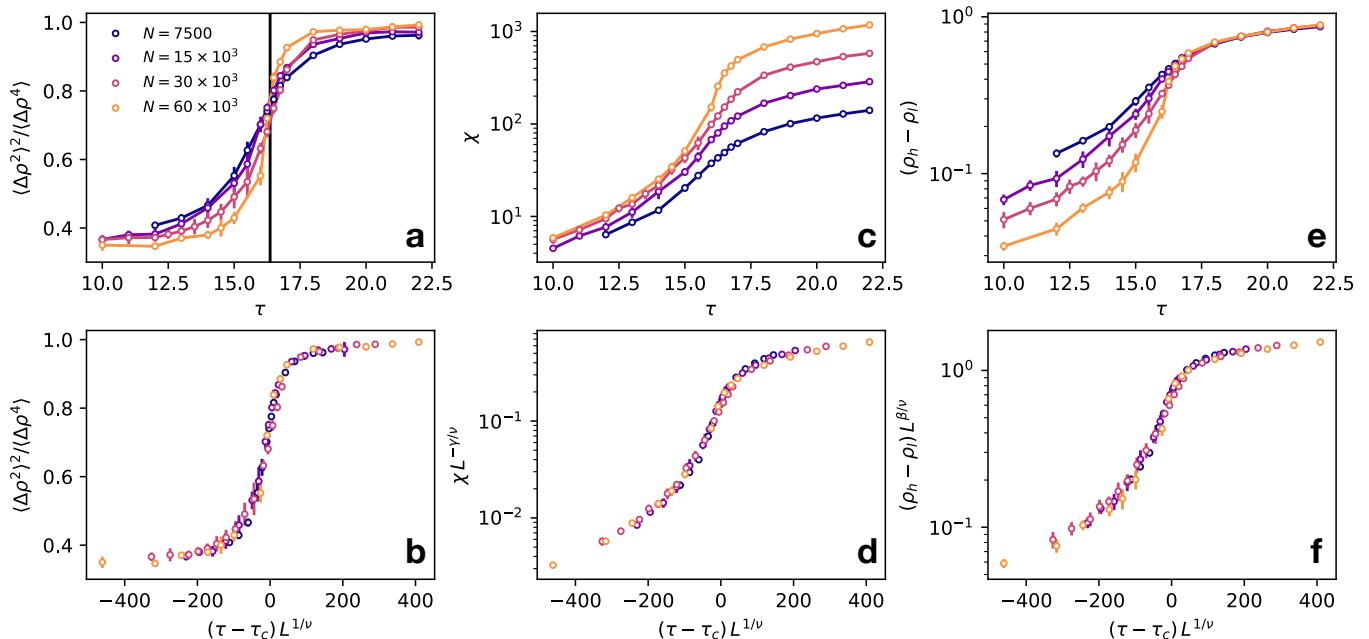


FIG. 2. FSS analysis. (a) Binder parameter for different system sizes. The intersection of the curves allows to locate τ_c (vertical line). (b) Data collapse of data in (a) as a function of the scaling variable $(\tau - \tau_c)L^{1/\nu}$ with $\nu = 1$. (c) Susceptibility χ as a function of τ for different system sizes. (d) collapse of data in (c) onto a universal scaling function with the exponents $\gamma = 7/4$ and $\nu = 1$. (e) order parameter for different system sizes. (f) data collapse of (e) with the exponents $\beta = 1/8$ and $\nu = 1$. Color code is the same for all panels (see legend in (a)).

of \mathcal{O} measured for different sizes should collapse onto each other when $L^{-\zeta_{\mathcal{O}}/\nu}\mathcal{O}$ is plotted as a function of $L^{1/\nu}(\tau - \tau_c)$.

A particularly interesting observable is the fourth order cumulant of density fluctuations $\langle \Delta \rho^2 \rangle^2 / \langle \Delta \rho^4 \rangle$ (the Binder parameter [30–32]), where brackets indicate averages over configurations and over sub-boxes. The density fluctuations are computed in the four $L \times L$ sub-boxes described above, specifically $\langle \Delta \rho^2 \rangle = \langle (N_b/L^2 - \langle N_b/L^2 \rangle)^2 \rangle$ where N_b is the number of particles found in one single sub-box. For the Binder parameter we expect $\zeta_{\mathcal{O}} = 0$ and thus it should be size-independent at $\tau = \tau_c$. Exploiting this property we locate $\tau_c \approx 16.36$ as the intersection the data for $N = 15 \times 10^3$ and $N = 60 \times 10^3$ (Fig. 2(a)). We choose to use these two sizes because $N = 60 \times 10^3$ is the largest size simulated and $N = 15 \times 10^3$ has a linear size which is two times smaller than the largest size. Note that this τ_c is approximately the value of τ at which cumulants of all sizes cross. Fig. 2(b) shows a good data collapse of the Binder parameter computed for different system sizes if we use the Ising exponent $\nu = 1$. An alternative way [21] to confirm $\nu = 1$ is to consider the size dependence of the slope of the cumulant at $\tau = \tau_c$. This study is reported in the SM showing that also this method yields $\nu \approx 1$.

In Fig. 2(c) we test the scaling of the susceptibility $\chi = \langle (N_b - \langle N_b \rangle)^2 \rangle / \langle N_b \rangle$ with Eq. (3). As one can see, the scaling is very good using the Ising critical exponent $\gamma = 7/4$. In addition we show in the SM that, monitoring the growth of χ near τ_c as a function of the size, we

obtain a value of γ which is very close to the Ising critical exponent. Note also that the χ in Fig. 2(c) does not show the typical peaked shape of the Ising model. This is due to the fact that the χ is obtained here by averaging together the values of N_b both in the dense and diluted phase. We have checked that the χ (computed in the same way) for the $2d$ critical lattice gas shows a similar s-shaped curve as a function of the inverse temperature and that this scales with $\gamma = 7/4$, as shown in the SM.

Furthermore, in Fig. 2(e) we consider the density difference between the boxes centered in the high and low-density phases $(\rho_h - \rho_l)$ (see Fig. 1(d)), which corresponds to the order parameter of the system. We find that this quantity displays a good scaling as observed in Fig. 2(f) with an exponent $\beta = 1/8$ of the Ising universality class. It is worth to stress that, in the thermodynamic limit, the order parameter would be different from zero only for $\tau > \tau_c$. It is however expected that, for finite systems, a smooth variation of the order parameter should be found also below τ_c and that this should scale with the appropriate exponent. We have also checked that $(\rho_h - \rho_l)$, computed as in the active system, scales with $\beta = 1/8$ in the case of the $2d$ equilibrium lattice gas for temperatures above the critical temperature (see SM for details).

Finally, we check if our results are consistent with the Ising exponent $\eta = 1/4$ which controls the decay of the static structure factor $S(k)$ near the critical point, i.e. $S(k) \sim k^{-2+\eta}$. To this aim we compute $S(k) = A \langle \rho_{\mathbf{k}}^* \rho_{\mathbf{k}} \rangle$ where $\rho_{\mathbf{k}}$ is the Fourier transform of the density fluctu-

ations and the normalization factor A is chosen so that $S(0) = \langle \Delta N^2 \rangle / \langle N \rangle$ (N being the fluctuating number of particles in the sub-system considered). To avoid the interfaces and focus only onto the bulk phase we compute the $S(k)$ for the particles in the diluted phase considering only those particles having $|x - L_x/4| < L/2$, i.e. all particles in the left sub-boxes in Fig. 1(d). We show the resulting $S(k)$ in Fig. 3: close to criticality $S(k)$ becomes fairly linear in double log scale at low k . The data at low k are well fitted by the power law $k^{-2+\eta}$ with $\eta = 1/4$ (full line) which is appreciably different from the mean-field decay $S(k) \sim k^{-2}$ (dashed line).

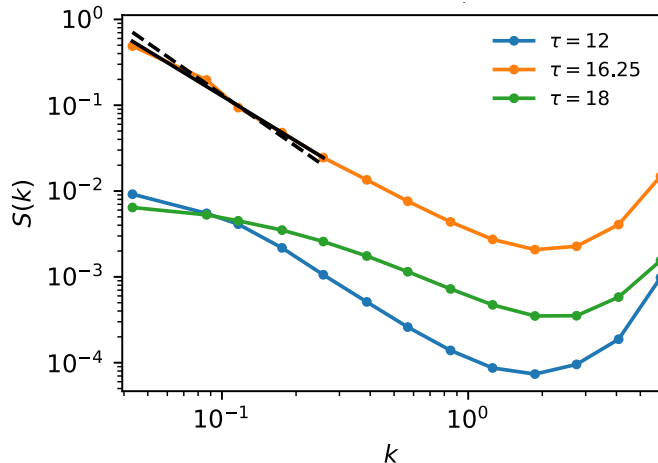


FIG. 3. Static structure factor $S(k)$ computed in the dilute phase for the largest system ($N = 60 \times 10^3$), different colors refer to different values of τ (see legend). Approaching the critical point the structure factor is well fitted by a power law $S(k) \sim k^{-2+\eta}$ at low k with $\eta = 1/4$ (full line). The best fit with $S(k) \sim k^{-2}$ (mean-field) is also shown as a dashed line for comparison.

Discussion and Conclusions. In this article, we have studied the critical properties of an active system undergoing MIPS in two spatial dimensions. Performing large-scale numerical simulations on GPU we have been able to demonstrate that the critical behavior of the system agrees well with the Ising universality class. Hence, all the static critical exponents satisfy the scaling relations. In particular we have shown that each observable of interest \mathcal{O} , developing a singularity at criticality in the thermodynamic limit, is well described by an opportune universal scaling function $G_{\mathcal{O}}$ as a function of the scaling variable $(\tau - \tau_c)L^{1/\nu}$.

It is worth to stress the importance of simulating large system sizes: previous studies on similar off-lattice active

models have reported different values of the critical exponents for system sizes smaller than those investigated in this work [21]. Although it has been speculated [12] that the limited sizes employed did not allow to observe the scaling regime, it is true that the similar sizes have been successfully exploited for the study of critical phenomena in passive attractive liquids, finding numerical results compatible with the Ising universality class [27]. We instead suspect that for those sizes another correlation length, different from the critical one, interferes with the scaling behaviour of the active system. In particular, it has been recently shown that the colored noise induces an effective coupling among particles velocities giving rise to “islands” of particles with correlated speed and orientation [33, 34]. Such correlation depends on τ , D and ρ but, importantly, does not diverge. We find that (see SM for discussion), close to the critical point, this correlation length is comparable with the size of the sub-boxes employed for the FSS analysis when the system size is small ($N = 3750$ particles) justifying the choice of larger system sizes. For a size as small as $N = 3750$ we find that the crossing point of the Binder cumulant happens at quite low values, although a reasonable scaling is found also for this size (see SM).

Our large-scale simulation results are consistent with the fact that, although the mechanism leading to MIPS is truly non-equilibrium, approaching the critical point any local non-equilibrium interaction becomes irrelevant. On the other hand, away from criticality, deviations from equilibrium might become important. For instance, deep in the phase separated region, non-equilibrium contribution (that cannot be described by any free-energy functional) can play a role in pattern formation marking a difference with respect to gas-liquid phase separation [20, 35–38].

These results can be relevant also for understanding and manipulating biological microswimmers. For these swimming cells the control parameters, i.e. the persistence time and the speed of the self-propulsion, are internal variables that each active agent could tune. This means that, through feedback with the environment, active systems might self-adjust the relevant parameters for reaching criticality, and thus develop self-organization [39].

Acknowledgments. EZ and NG acknowledge financial support from the European Research Council (ERC Consolidator Grant 681597, MIMIC). MP acknowledges financial support from the H2020 program and from the Secretary of Universities and Research of the Government of Catalonia through Beatriu de Pinós program Grant No. 2018 BP 00088.

[1] L. Kadanoff, Critical behavior, universality and scaling in critical phenomena (1971).

[2] M. C. Marchetti, J. F. Joanny, S. Ramaswamy, T. B. Liverpool, J. Prost, M. Rao, and R. A. Simha, Hydrodynamics of soft active matter, *Rev. Mod. Phys.* **85**, 1143

- (2013).
- [3] C. Bechinger, R. Di Leonardo, H. Löwen, C. Reichhardt, G. Volpe, and G. Volpe, Active particles in complex and crowded environments, *Rev. Mod. Phys.* **88**, 045006 (2016).
 - [4] A. Klopfer, Physics of living systems, *Nature Physics* **14**, 645 (2018).
 - [5] J. Tailleur and M. E. Cates, Statistical mechanics of interacting run-and-tumble bacteria, *Phys. Rev. Lett.* **100**, 218103 (2008).
 - [6] M. E. Cates and J. Tailleur, Motility-induced phase separation, *Annu. Rev. Condens. Matter Phys.* **6**, 219 (2015).
 - [7] G. Liu, A. Patch, F. Bahar, D. Yllanes, R. D. Welch, M. C. Marchetti, S. Thutupalli, and J. W. Shaevitz, Self-driven phase transitions drive myxococcus xanthus fruiting body formation, *Phys. Rev. Lett.* **122**, 248102 (2019).
 - [8] H. B. Callen, *Thermodynamics and an introduction to thermostatistics* (1998).
 - [9] C. Domb, *Phase transitions and critical phenomena* (Elsevier, 2000).
 - [10] M. Paoluzzi, C. Maggi, and A. Crisanti, Statistical field theory and effective action method for scalar active matter, *Phys. Rev. Research* **2**, 023207 (2020).
 - [11] M. Paoluzzi, C. Maggi, U. Marini Bettolo Marconi, and N. Gnan, Critical phenomena in active matter, *Phys. Rev. E* **94**, 052602 (2016).
 - [12] B. Partridge and C. F. Lee, Critical motility-induced phase separation belongs to the ising universality class, *Phys. Rev. Lett.* **123**, 068002 (2019).
 - [13] J. Stenhammar, D. Marenduzzo, R. J. Allen, and M. E. Cates, Phase behaviour of active brownian particles: the role of dimensionality, *Soft Matter* **10**, 1489 (2014).
 - [14] A. Patch, D. Yllanes, and M. C. Marchetti, Kinetics of motility-induced phase separation and swim pressure, *Phys. Rev. E* **95**, 012601 (2017).
 - [15] Y. Fily and M. C. Marchetti, Athermal phase separation of self-propelled particles with no alignment, *Phys. Rev. Lett.* **108**, 235702 (2012).
 - [16] D. Levis, J. Codina, and I. Pagonabarraga, Active brownian equation of state: metastability and phase coexistence, *Soft Matter* **13**, 8113 (2017).
 - [17] A. Patch, D. M. Sussman, D. Yllanes, and M. C. Marchetti, Curvature-dependent tension and tangential flows at the interface of motility-induced phases, *Soft matter* **14**, 7435 (2018).
 - [18] S. Hermann, P. Krinninger, D. de las Heras, and M. Schmidt, Phase coexistence of active brownian particles, *Phys. Rev. E* **100**, 052604 (2019).
 - [19] P. Digregorio, D. Levis, A. Suma, L. F. Cugliandolo, G. Gonnella, and I. Pagonabarraga, Full phase diagram of active brownian disks: From melting to motility-induced phase separation, *Phys. Rev. Lett.* **121**, 098003 (2018).
 - [20] S. Mandal, B. Liebchen, and H. Löwen, Motility-induced temperature difference in coexisting phases, *Physical Review Letters* **123**, 228001 (2019).
 - [21] J. T. Siebert, F. Dittrich, F. Schmid, K. Binder, T. Speck, and P. Virnau, Critical behavior of active brownian particles, *Physical Review E* **98**, 030601 (2018).
 - [22] C. Maggi, U. M. B. Marconi, N. Gnan, and R. Di Leonardo, Multidimensional stationary probability distribution for interacting active particles, *Scientific reports* **5** (2015).
 - [23] G. Szamel, E. Flenner, and L. Berthier, Glassy dynamics of athermal self-propelled particles: Computer simulations and a nonequilibrium microscopic theory, *Physical Review E* **91**, 062304 (2015).
 - [24] E. Fodor, C. Nardini, M. E. Cates, J. Tailleur, P. Visco, and F. van Wijland, How far from equilibrium is active matter?, *Phys. Rev. Lett.* **117**, 038103 (2016).
 - [25] S. Dal Cengio, D. Levis, and I. Pagonabarraga, Linear response theory and green-kubo relations for active matter, *Physical Review Letters* **123**, 238003 (2019).
 - [26] L. L. Bonilla, Active ornstein-uhlenbeck particles, *Physical Review E* **100**, 022601 (2019).
 - [27] M. Rovere, P. Nielaba, and K. Binder, Simulation studies of gas-liquid transitions in two dimensions via a subsystem-block-density distribution analysis, *Zeitschrift für Physik B Condensed Matter* **90**, 215 (1993).
 - [28] L. Bai and D. Breen, Calculating center of mass in an unbounded 2d environment, *Journal of Graphics Tools* **13**, 53 (2008).
 - [29] D. J. Amit and V. Martin-Mayor, *Field Theory, the Renormalization Group, and Critical Phenomena: Graphs to Computers Third Edition* (World Scientific Publishing Company, 2005).
 - [30] K. Binder, Finite size scaling analysis of ising model block distribution functions, *Zeitschrift für Physik B Condensed Matter* **43**, 119 (1981).
 - [31] M. Rovere, D. Hermann, and K. Binder, Block density distribution function analysis of two-dimensional lennard-jones fluids, *EPL (Europhysics Letters)* **6**, 585 (1988).
 - [32] M. Rovere, D. W. Heermann, and K. Binder, The gas-liquid transition of the two-dimensional lennard-jones fluid, *Journal of Physics: Condensed Matter* **2**, 7009 (1990).
 - [33] L. Caprini, U. M. B. Marconi, and A. Puglisi, Spontaneous velocity alignment in motility-induced phase separation, *Physical Review Letters* **124**, 078001 (2020).
 - [34] L. Caprini, U. M. B. Marconi, C. Maggi, M. Paoluzzi, and A. Puglisi, Hidden velocity ordering in dense suspensions of self-propelled disks, *Physical Review Research* **2**, 023321 (2020).
 - [35] R. Wittkowski, A. Tiribocchi, J. Stenhammar, R. J. Allen, D. Marenduzzo, and M. E. Cates, Scalar φ 4 field theory for active-particle phase separation, *Nature communications* **5**, 4351 (2014).
 - [36] C. Nardini, É. Fodor, E. Tjhung, F. Van Wijland, J. Tailleur, and M. E. Cates, Entropy production in field theories without time-reversal symmetry: quantifying the non-equilibrium character of active matter, *Physical Review X* **7**, 021007 (2017).
 - [37] R. Singh and M. E. Cates, Hydrodynamically interrupted droplet growth in scalar active matter, *Phys. Rev. Lett.* **123**, 148005 (2019).
 - [38] E. Tjhung, C. Nardini, and M. E. Cates, Cluster phases and bubbly phase separation in active fluids: Reversal of the ostwald process, *Phys. Rev. X* **8**, 031080 (2018).
 - [39] A. Cavagna, A. Cimorelli, I. Giardina, G. Parisi, R. Santagati, F. Stefanini, and M. Viale, Scale-free correlations in starling flocks, *Proceedings of the National Academy of Sciences* **107**, 11865 (2010).
 - [40] A. Bovier and F. den Hollander, *Kawasaki dynamics, in Metastability* (Springer, 2015) pp. 425–457.
 - [41] L. Zhi-Huan, L. Mushtaq, L. Yan, and L. Jian-Rong, Critical behaviour of the ferromagnetic ising model on a triangular lattice, *Chinese Physics B* **18**, 2696 (2009).

SUPPLEMENTAL MATERIAL

Equilibration time and length of the simulation runs

We show here that the length of the simulation runs is long enough to allow the full relaxation of the density correlation function $C(t) = \langle \Delta N_b(0) \Delta N_b(t) \rangle / \langle \Delta N_b^2 \rangle$, where $\Delta N_b = N_b - \langle N_b \rangle$ is the fluctuation of the number of particles in the sub-box. More specifically we analyze separately the relaxation in the dense and diluted phases considering the two sub-boxes on the left and two on the right as shown in Fig 1 of the main text. Figure 4(a) and (b) display $C(t)$ for the largest system investigate (i.e $N = 60000$) at different τ values both in the dense and diluted phase: in both cases $C(t)$ decay to zero at all τ .

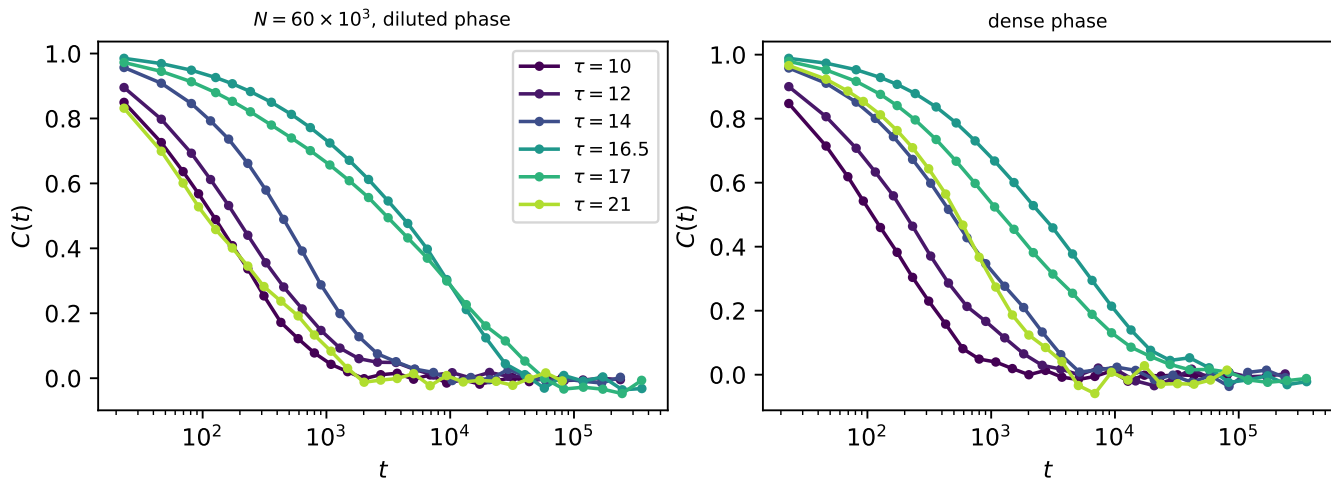


FIG. 4. Density auto-correlation function for the system with $N = 60000$ particles at $\rho = 0.95$ and different values of τ . Left panel: diluted phase. Right panel: dense phase.

Averages and error estimation

All quantities appearing in the main text (i.e. the Binder cumulant, the susceptibility and the order parameter) are averaged over 16000 to 36000 configurations and over all sub-boxes. Individual configurations are taken at time intervals of duration ≈ 23 , which is approximately equal largest τ explored. Moreover for the values of τ close to τ_c these quantities of interest are averaged over multiple initial random configurations (up to 12 for the largest system sizes).

To estimate the error on these quantities we proceed as follows: we first divide each run in time windows larger than the relaxation time of the density correlation function $C(t)$ (Fig. 4) we then compute the observable in each time-window and compute the standard error of the mean over all time windows. In Fig. 2 of the main text we report the error as twice the standard error of the mean. We have also checked that by computing the average of the Binder cumulant over these time windows (instead that on all configurations) we get almost identical results than those reported in Fig. 2 of the main text.

Estimate of the critical density

We roughly estimate the critical density by performing a density scan in the proximity of the critical point for the smallest system investigated (i.e. for $N = 3750$). This is done by studying the evolution of the Binder cumulant as a function of ρ as shown in Fig. 5. Following Ref. [32] we estimate the critical density locating the maximum of Fig. 5. To extract such value we have interpolated with a 2nd order polynomial the closest six points to the maximum of the curve finding $\rho_c \approx 0.95$. We use this value for all the sizes discussed in the main text neglecting the dependence of ρ_c on the size of the system.

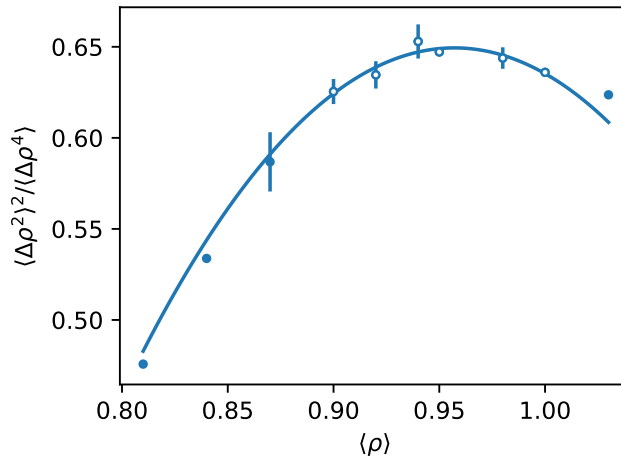


FIG. 5. Fourth order cumulant as a function of density. Data points represent the Binder parameter varying the density at fixed $\tau = 16$ and $N = 3750$. The open symbols are the six point closest to the maximum used for fitting with a parabola (full line) determining ρ_c .

Alternative estimates of the critical exponents

Following Ref. [21] we also try to determine the critical exponents ν and γ as follows. We first focus on the dependence of the slope of the critical Binder cumulant on L that, according to FSS, scales as

$$\left[\frac{\partial}{\partial \tau} \left(\frac{\langle \Delta \rho^2 \rangle^2}{\langle \Delta \rho^4 \rangle} \right) \right]_{\tau=\tau_c} \sim L^{1/\nu} \quad (4)$$

To check Eq. (4) we evaluate the derivative of the cumulant by fitting the numerical data with a generalized logistic function of the form

$$y(\tau) = A_1 + \frac{A_2}{[A_3 + A_4 e^{-(\tau-\tau_0)}]^{1/\theta}} \quad (5)$$

Where $A_1, A_2, A_3, A_4, \tau_0$ and θ are fitting parameters. As shown in Fig. 4(a) this function fits well the data especially around τ_c and allows us to estimate the derivative (4). This derivative is reported in Fig. 4(b) as a function of the system size and it is effectively well fitted by $\sim L^{1/\nu}$ with $\nu = 1$. In fact a direct fit with a power law gives $\nu \approx 1.03$. Contrarily the best fit with the exponent $\nu = 1.5$ proposed in Ref. [21] deviates considerably from the data.

Next we consider the size dependence of the susceptibility χ at τ_c (i.e. $\chi_{\tau=\tau_c}$), that should scale as $\chi_{\tau=\tau_c} \sim L^{\gamma/\nu}$. To do this we simply linearly interpolate the χ at τ_c at all sizes and report the results in Fig. 4(c). This quantity is also well fitted by the Ising exponent $\gamma/\nu = 7/4 = 1.75$. A direct fit with a power law yields $\gamma/\nu \approx 1.80$ which is only about $\sim 3\%$ larger than the Ising value. Also in this case by fixing the values of $\gamma = 2.2$ and $\tau = 1.5$ (i.e. $\gamma/\nu \approx 1.47$) from Ref. [21] we obtain a worse fit of our data.

Scaling behavior of the susceptibility and of the order parameter in the 2d equilibrium lattice gas

To check whether the susceptibility and the order parameter behave in the same qualitative way in the active system and in equilibrium we consider a lattice gas on a triangular lattice in a rectangular geometry (similar to the one employed for the active system). We simulate systems of three different sizes composed by $N = 192, 768$ and 3072 sites. These sites are enclosed in a rectangular box of size $(0, L_x) \times (0, L_y)$ with $L_x = a N_x$ and $L_y = a\sqrt{3}N_y/2$, where $a = 1$ is the lattice spacing. In all simulations we set $N_x = 3 N_y$ and $N = N_x \times N_y$ is the total number of sites. Some near-critical configurations lattice gas simulated is shown in Fig. 7(a) and (b). By imposing periodic boundary conditions every site has 6 neighbours and the total lattice gas Hamiltonian (H_{lg}) is given by

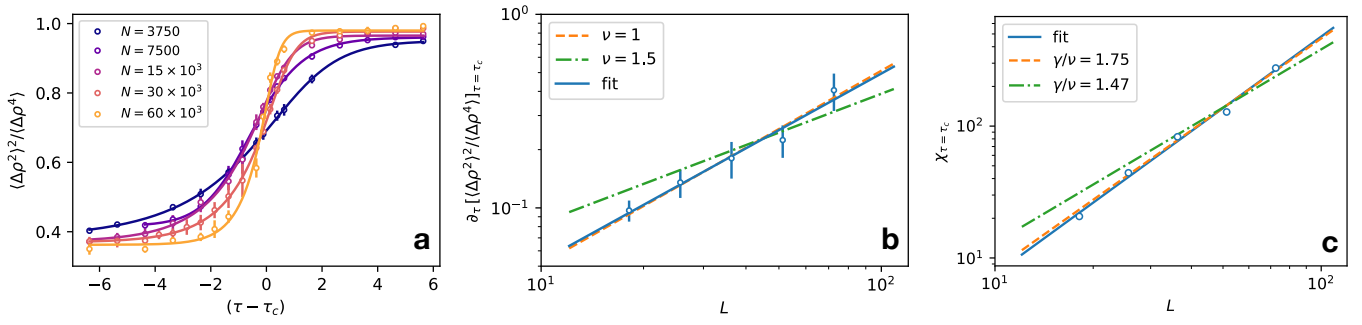


FIG. 6. (a) Fits of the Binder cumulant for estimating its derivative near τ_c . (b) Slope of the cumulants as a function of size. Solid line is the best fit of data points which gives $\nu = 1.03$. Orange dashed line is the best fit fixing $\nu = 1$ while green dashed-dotted line is the best fit with $\nu = 1.5$ from Ref. [21]. (c) susceptibility as a function of size. Solid line is the best fit of data points which gives $\gamma/\nu = 1.80$. Orange dashed line is the best fit fixing $\gamma/\nu = 1.75$ while the green dashed-dotted line is the fit with $\gamma/\nu = 1.47$ taken from Ref. [21].

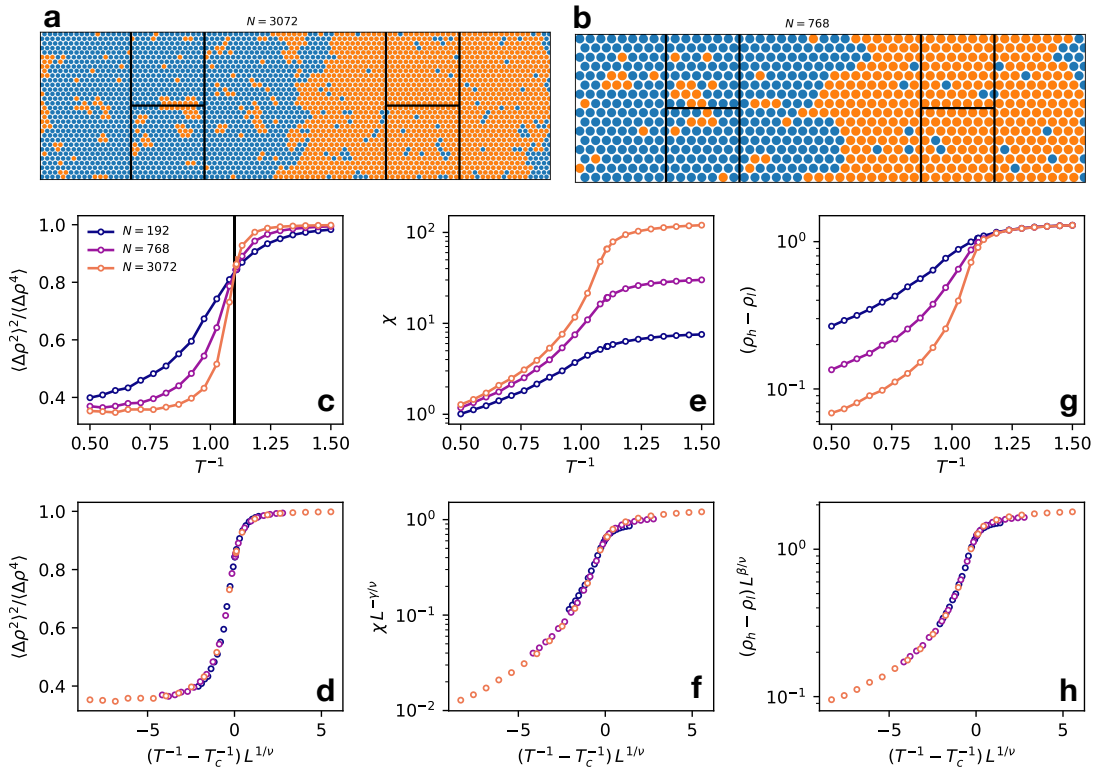


FIG. 7. (a) and (b) Near-critical configurations of an equilibrium lattice gas on the triangular lattice in a rectangular geometry for two different sizes (at $T^{-1} \approx 1.13$). Blue points represent empty sites while orange points represent occupied sites. The configuration is shifted so that the dense phase is centered on the right boxes (located at $x = 3L_x/4$, black lines) and the diluted phase is centered on the left sub-boxes (at $x = L_x/4$). (c) Binder cumulant for the lattice gas as a function of inverse temperature for different sizes (see legend), the vertical line corresponds to the exact $T_c^{-1} \approx 1.1$. (d) Data collapse of the data in (c) with $\nu = 1$. (e) Susceptibility for the lattice gas as a function of inverse temperature for different sizes. (f) Data collapse of the data in (e) with $\nu = 1$ and $\gamma = 7/4$. (g) Order parameter as a function of the inverse temperature for the lattice gas for various sizes indicated in the legend (the order parameter is computed as the average density difference between the sub-boxes on the right and on the left). (h) Data collapse of the data in (h) using the exponents $\beta = 1/8$ and $\nu = 1$.

$$H_{\text{lg}} = -J \sum_{\langle i,j \rangle} n_i n_j, \quad (6)$$

where J is the coupling constant set to 1 for convenience and n_i is the occupancy of the i -th site which assume

the values 0 or 1. The simulations conserve the total occupancy (i.e. $\sum_i n_i = \text{const}$) by using a Kawasaki-type dynamics [40] in which a site can exchange its occupancy with any other site in the lattice in order to accelerate the approach to equilibrium. After an occupancy switch is proposed a standard Monte Carlo (MC) Metropolis rule is applied and the new configuration is accepted or rejected according to the energy change. All simulation results are obtained at fixed average occupancy $\sum_i n_i/N = 0.5$ (i.e. at the critical occupancy), starting from a random configuration (i.e. at infinite temperature). It is possible to show, via the transformation $n_i = (1 + \sigma_i)/2$, that the model (6) can be mapped onto the Ising model with spin $\sigma_i = \pm 1$ on the triangular lattice having critical temperature $T_c = 4/\ln 3 \approx 3.641$ (for $J = 1$ and $k_B = 1$) [41]. As a consequence, the T_c of the lattice gas model turns out to be $T_c = 1/(\ln 3) \approx 0.91$, i.e. an inverse critical temperature $T_c^{-1} \approx 1.099$ while the critical average occupancy is $n_c = 0.5$.

The configurations of the lattice gas are analyzed as described in the main text for the active system. We start by shifting each configuration so that its center of mass is positioned at $x = 3L_x/4$ as also shown in Fig. 7(a) and (b). Subsequently the quantities of interest are averaged over all four $L \times L$ sub-boxes, where $L = L_y/2$. The density ρ in one sub-box is computed as $\rho = \sum'_i n_i/L^2$, where the prime indicates the sum runs only on those sites within the sub-box. Using this method we further check the correctness of the critical temperature by showing the Binder parameter and its good scaling with $\nu = 1$ in Figs 7(c) and (d). In the main text we have mentioned that the χ , computed by averaging over all sub-boxes, does not show the typical peaked shape but rather forms a s-shaped curve when plotted as a function of the control parameter. This is the case also for the equilibrium lattice gas as shown in Fig. 7(e). In Fig. 7(f) we also show that this χ scales well with $\nu = 1$ and $\gamma = 7/4$. In the main text we have also used the average difference of the density in the high-density phase ρ_h and of the low-density phase ρ_l as an order parameter. To check if this quantity behaves as expected at criticality also in the equilibrium case we compute ρ_h and ρ_l as the average density of the two sub-boxes on the right and on the left respectively. The resulting $(\rho_h - \rho_l)$ is shown in Fig. 7(b) as a function of T^{-1} . In Fig. 7(c) we show that we obtain a good data collapse by using the Ising exponents $\beta = 1/8$ and $\nu = 1$. These data are clearly compatible with those presented for the off-lattice active system discussed in the main text, thus reinforcing the robustness of the analysis bringing to the Ising universality class in the case of the active system.

System sizes and velocity correlation length

We discuss here the data collapse for the smallest system simulated, i.e. $N = 3750$ (not included in the main text), which is comparable with the sizes used in a previous investigation on the critical behaviour of an off-lattice active system [21]. In Fig. 8 we report the data for this size for the cumulant, the susceptibility and the order parameter. It is evident that a reasonable data collapse with the Ising exponents is found also for $N = 3750$ (see Fig. 8(b),(d) and (f)). However the crossing point of the Binder cumulant for this size seems significantly lower in height and τ than the larger sizes.

As mentioned in the main text we speculate that this could be due to the presence of other correlations induced by the non-equilibrium propulsion force. Recent works [33, 34] have shown that in active systems the colored noise induces an effective coupling between particles velocities. This effect gives rise to regions of densely packed particles with correlated speed and velocity orientation. Figure 9 shows the orientation map of particle velocities for different system sizes, including $N = 3750$. The red boxes shown in the figure are the sub-boxes employed for the finite size scaling analysis. It is clear that for the smallest system the “islands” of velocity-correlated particles have a size almost comparable with the size of the sub-boxes as also magnified in Fig. 9. Contrarily, on increasing the system size, the sub-boxes become much larger than the velocity correlation length, which does not diverge and thus becomes independent on the system sizes shown here (as expected also from the theory presented in Ref.s [33, 34]). However future careful investigations need to be carried on to clarify the influence of velocity correlations in FFS analysis.

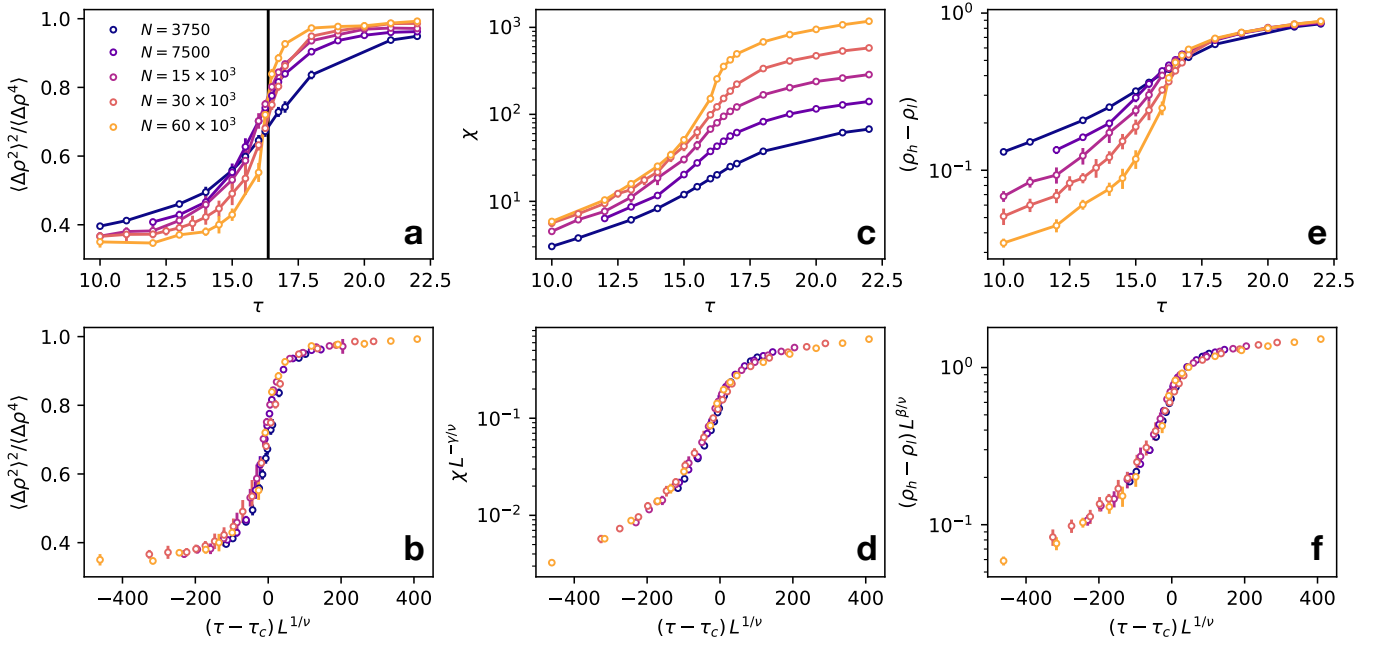


FIG. 8. Data collapse of the analyzed quantities including the smallest system with size $N = 3750$.

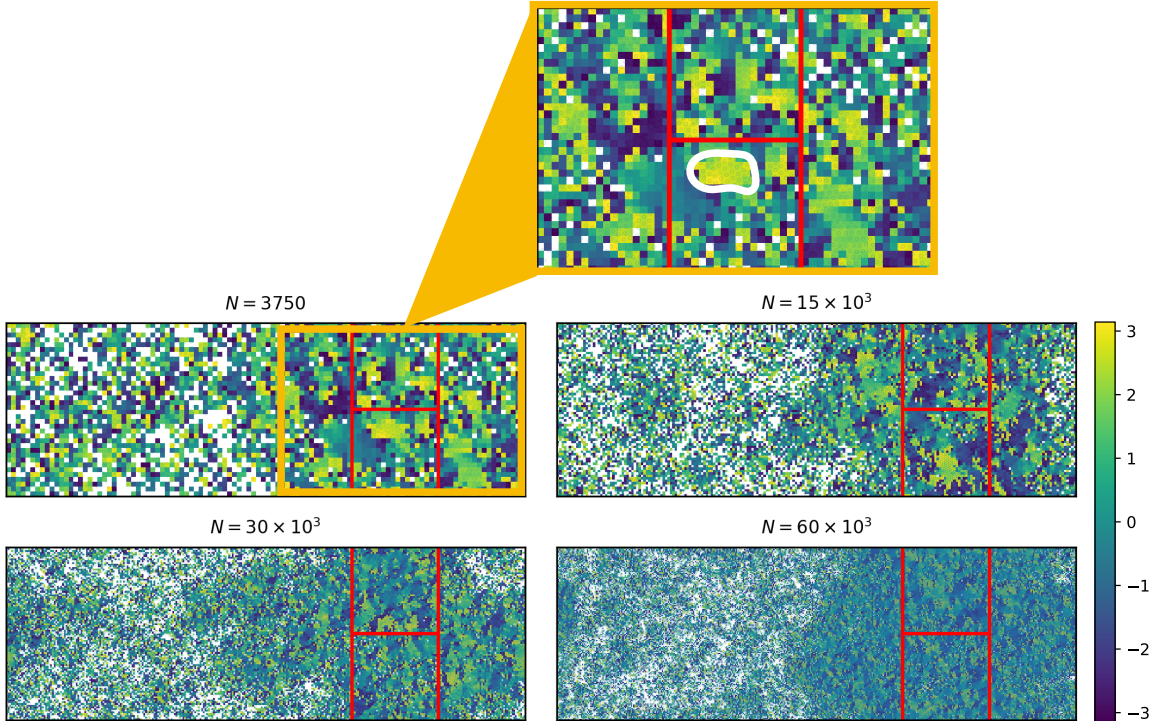


FIG. 9. Velocity orientation map for several system sizes, with $\tau = 16.5$ and $\rho = 0.95$. The map is calculated for a single configuration choosing bins of the order of the particles size. Different colors represent different particle orientations from $-\pi$ (violet) to π (yellow), see colorbar on the right. White pixels correspond to bins where no particles are found. Red boxes are drawn to show the sub-box size employed for the FSS analysis. The orange panel is a magnification of the dense phase for $N = 3750$ where a region of correlated velocities is contoured in white to better visualize its size.